Research Article

Qihang Xv, Gan Tian*, Wei Zhang, Zhengwei Yang, and Anbo Ming

Effect of the weld parameter strategy on mechanical properties of double-sided laser-welded 2195 Al-Li alloy joints with filler wire

https://doi.org/10.1515/htmp-2021-0043 received August 11, 2021; accepted November 05, 2021

Abstract: Compared with single-sided welding, doublesided welding can melt through thicker workpieces and improve the mechanical performance of the weld. In this work, laser welding with filler wire of 2195 Al-Li alloy plates is conducted via double-sided out-of-sync welding. By combining experiment and numerical simulation results, the influence laws of the weld's mechanical properties are studied by considering the condition of both sides under different welding parameters. The results show that the welding speed is the key parameter determining the heat input of the weld. In the welds fabricated at slow welding speeds, the cooling rate is greater, resulting in accelerated solidification. The weld solidifies before hydrogen overflows from the weld pool, resulting in increased pore density and weakened mechanical properties. Therefore, welding parameters determine the heat input of the weld and subsequently the mechanical properties. It is shown that a special double-sided welding strategy can effectively control the heat input. Specifically, in contrast to those of the first, the welding parameters of the second side of the weld reduce the wire feeding speed when other parameters are held constant. Compared with the process strategy using identical double-sided parameters, this can slightly increase the heat input and reduce the defects in the weld, which can improve its mechanical properties. In the comparative experiment, the wire feeding speed was reduced from 5 to 3 mm·s⁻¹, and the tensile strength of the weld was increased by 10%.

Keywords: laser welding, double-sided welding, feeding wire, weld pool, filler wire

Anbo Ming: School of Mechanics, Civil Engineering and Architecture, Northwestern Polytechnical University, Xi'an 710025, China

1 Introduction

2195 Al–Li alloys are a new generation of Al–Li alloy; however, their poor welding performances limit their application. Low heat input welding (e.g., friction stir welding, laser welding, and electron beam welding methods) represent promising techniques for the welding of Al–Li alloys; these techniques are characterized by high energy concentrations, narrow weld regions, and deformation [1–12]. Among these welding techniques, laser welding represents an emerging welding method owing to its prominent advantages in the above-mentioned characteristics. Studying the process parameters of 2195 Al–Li alloy laser welding is of great significance for improving its weld performance.

The energy of laser welding is relatively concentrated; hence, 2195 Al-Li alloys have high reflectivity. When the butt joints of the workpiece are welded, a single-sided welding process requires a higher welding power to ensure penetration. Compared with single-sided welding, double-sided welding can penetrate the weld with lower heat input and thereby achieve superior mechanical properties. Double-sided welding does not need to penetrate the thick plate at a single time; hence, a smaller energy input can be used, which reduces the residual stress of the joint and alleviates grain coarsening to some extent. Meanwhile, the back side of the double-sided welding has a tempering effect on the other welded side, which can refine the coarse grains of the fusion zone (FZ) and heat affect zone (HAZ) on that side and release part of the welding stress. In addition, elements with low boiling points in Al-Li alloys are easy to evaporate, resulting in a decrease in the weld strength. Feeding wire can improve this property of the weld.

In the past, research into double-sided welding has mainly focused on friction stir welding, arc welding, and T-joint welding. A few studies have applied laser welding techniques to flat plate butt double-sided welding tasks. Farrokhi experimentally studied the influence of welding speed on the solidification cracking of double-sided

^{*} Corresponding author: Gan Tian, Xi'an Research Institute of High-Tech, Xi'an 710025, China, e-mail: Tiangan_2012@outlook.com Qihang Xv, Wei Zhang, Zhengwei Yang: Xi'an Research Institute of High-Tech, Xi'an 710025, China

welding [13]. The research into double-sided arc welding has mainly focused on the different welding methods used on both sides. Zhou et al. established a three-dimensional transient numerical model of a double-sided tungsten-inert-gas-metal-inert-gas (TIG-MIG) pool to identify its heat transfer process [14]. Wu et al. established a numerical model for the flow and heat transfer of the weld pool of double-sided arc welding and they calculated the geometry of the keyhole and weld pool [15]. Dong et al. established a three-dimensional steady-state numerical model of the melting PA-gas-tungsten-arc (PA-GTA) double-sided welding melting process, and they calculated the fluid flow and temperature field distribution [16]. The results show that the peak temperature and temperature gradient of the weld pool on the PA side were higher than those on the GTA side. Luo et al. studied the application of double-sided submerged arc welding to duplex stainless steel, and they analyzed the effectiveness of the double-sided welding process, the phase distribution characteristics, and the mechanical properties of the welded joints [17]. Through experiments, Lei et al. conducted a comparative study on the single-arc welding and laser-arc double-sided welding processes in terms of the geometry of the welded joints, the weld morphology, and mechanical properties [18]. It was found that laser arc double-sided welding significantly improved the performances of welded joints [18]. Hejazi and Mirsalehi compared two-sided friction stir welding with its traditional single-side counterpart under an AA6061 sheet by using different lengths of stir needles [19]. It was found that the mechanical properties of the double-sided friction stir welding joints were superior [19]. Jiang et al. performed laser-MIG composite double-sided welding on an Al 5083 alloy laser with a thickness of 30 mm, and they found that the cladding of the MIG welding played a role in making up for weld formation, eliminating the pores caused by small holes, and refining grains [20]. Tuncel and Aydin found that the welding type and pulse frequency had a significant effect on tensile properties, and the tensile properties of double-sided laser welded joints significantly outperformed those of single-sided ones [21].

In this study, to improve the weld performance, double-sided laser welding with filler wire was applied to a 2195 Al–Li alloy workpiece. In double-sided laser wire-filling welding, the welding parameters have a sizeable impact on the weld performance. To explore the effects of the different welding parameter settings on the weld microstructure and mechanical properties of butt plate joints, we conducted numerical simulations and experiments. In this work, the flow and heat transfer characteristics of the weld pool were simulated by a

computational fluid dynamics (CFD) method, in which the influence of wire filling on the weld pool was included. Numerical simulation results and mechanical weld properties have not been well studied together in the literature. In this experiment, different welding strategies were employed. The microstructures, hardnesses, and tensile strengths of welds were obtained from experiments. The distribution of pores and the microstructure and morphology of the weld were analyzed. In previous research, numerical simulation results and the mechanical properties and crystalline structures of the weld have only rarely been studied together. The flow field, thermal cycle curve, and cooling rate of the weld pool were obtained by numerical simulation. By combining the numerical and experimental results, the relationships between welding strategies, weld FZ characteristics, and mechanical properties were analyzed. A welding strategy to control the heat input and improve weld quality was proposed.

2 Design of experiments and materials

2.1 Materials and experimental procedure

Figure 1 shows a schematic diagram of laser double-sided welding with a filler wire. Because the laser welding energy is concentrated, the welding wire melts via heat transfer from the weld pool and flows thereinto. Meanwhile, the high reflectivity entails a large loss of laser energy on the surface of the workpiece; thus, only a very shallow keyhole can be formed, in contrast to deep penetration welding. The welding mode was that of thermal conduction welding.

In the experiment, the JK2003SM Nd:YAG laser produced a laser beam (wavelength: 1.06 µm) that was conducted to the laser head via an optical fiber and focused upon the surface of the workpiece via the lens. The spot diameter was 3 mm and the focal length was 160 mm; the flow rate for the shield gas was set to 15 L·min⁻¹. The Al–Li alloys feature a high reflectivity, and the filler wire can absorb a proportion of the laser energy. The process window of the Al–Li alloy was obtained after several experiments under the condition of 1,500 W power, and the process parameters of the 2195 Al–Li alloy laser wire filler weld (thickness: 2 mm) were formulated.

The workpiece was a 2195-T8 Al–Li alloy with a thickness of 2 mm. Before welding, the surface of the workpiece was cleaned and its surface roughness increased by

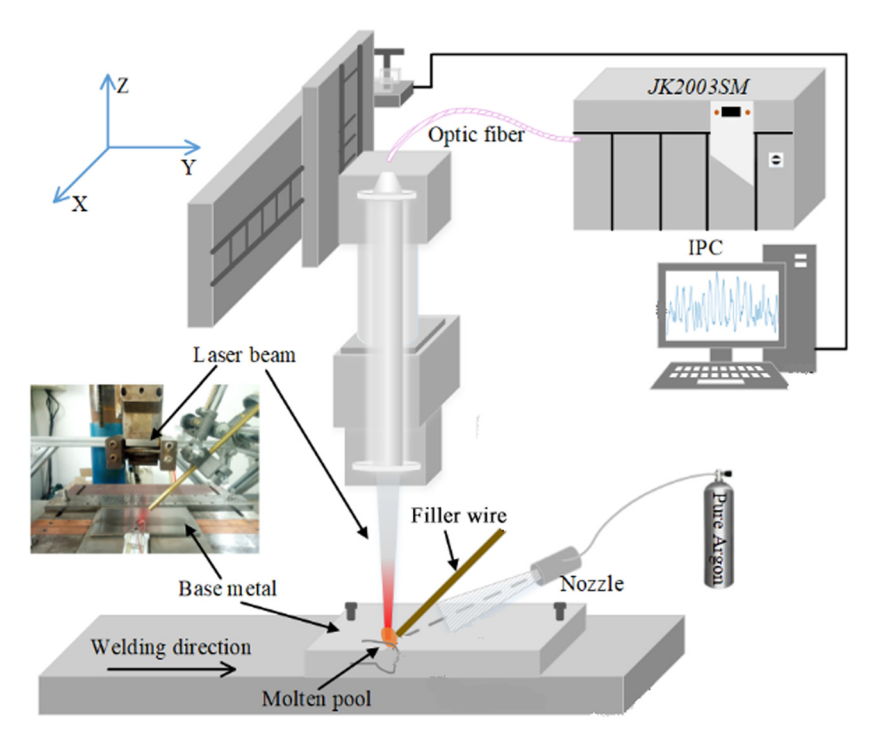


Figure 1: Schematic diagram of laser weld with filler wire.

mechanical polishing to reduce reflectivity. The work-piece size was $150 \, \text{mm} \times 100 \, \text{mm}$ and was fixed on the welding platform. An ER2319 wire (diameter: 1.2 mm) was installed in front of the welding direction relative to the focal point. The angle between the welding wire and workpiece plane was 45°, and the wire feeding device and laser were installed on the motion platform to facilitate movement. During the welding process, the welding wire was not directly irradiated by the laser focus but instead melted by thermal conduction through contact with the edge of the weld pool; this realized a stable liquid bridge transition mode. Table 1 shows the chemical composition of the welding wire and workpiece.

After the welding was completed, samples were taken from the cross section of the weld for characterization. Figure 2(a) depicts the sampling shape of the tensile sample, and Figure 2(b) represents the size of the tensile

sample. Then, the tensile properties of the specimens were tested with a tensile machine.

Two small pieces of samples were taken far from the deformation zone along the vertical weld direction for each weld sample to facilitate metallographic microstructure observation and hardness testing. After extraction, the sample was inlayed by the XBH-30 inlaying material and polished with metallographic sandpaper to make the sample surface smooth and scratch-free. Then, the sample was polished with diamond polishing paste (particle size: $1.5\,\mu m$). Next, corrosion was performed with a Keller reagent, and the weld microstructure was observed under a metallurgical microscope. The joint hardness was tested with a hardness tester, with a loading load of 100 gf and a loading time of 15 s. The universal tensile test machine was used for the mechanical performance experiment and the tensile speed was $2\,mm\cdot min^{-1}$.

Table 1: Chemical compositions of the workpiece and filler wire

Workpiece	Cu (%)	Li (%)	Ag (%)	Zr (%)	Fe (%	6)	Mg (%)	Ti (%)	Al
2195 alloy	3.7	0.8	0.2	0.1	0.1		0.2	0.068	Balance
Filler wire	Cu (%)	Fe (%)	Mn (%)	Mg (%)	Si (%)	Zn (%)	Ti (%)	V (%)	Al (%)
ER2319	5.6	0.3	0.3	0.2	0.2	0.1	0.15	0.1	Balance

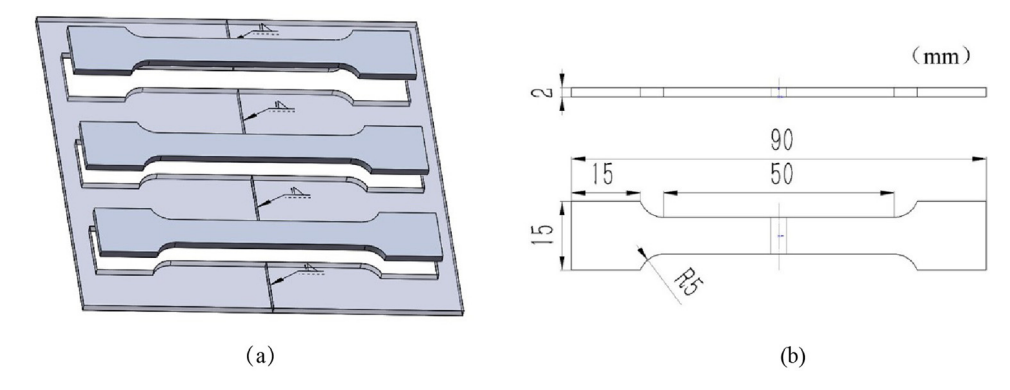


Figure 2: Sampling method. (a) tensile sample shape; (b) size of tensile sample.

2.2 Experimental design

To study the influence of different welding strategies on the mechanical properties of the welds, three experiments with different welding parameters were designed for comparison. In the experiment, the laser power, focal length, and focal radius were kept constant. Each group of experiments was performed twice. The welding parameters under the three welding strategies are shown in Table 2.

In the experimental design and, under a fixed power, the welding speed and wire feeding speed were the key variables affecting the heat input because they determine the heat inputted to the workpiece. In the experiment, the front-side welding was not performed simultaneously with that on the reverse side. Hence, the influence of the front and back sides of the workpiece on the weldings at different welding speeds and wire feeding speeds were considered. During the experiment, the laser welding (with filler wire) was first performed on the front of the workpiece; then, the workpiece was cooled to room temperature. Then, the back side of the workpiece was welded. Initially, welding experiments were conducted under multiple parameters, and the parameters of successful welding were selected to summarize the process window. During this process, it was found that when the welding speeds of the front and reverse were inconsistent and the spread of the welding wire was unstable, leading to a welding failure. Therefore, an experiment using

different welding speeds on the front and back sides was eliminated, and three experimental parameters were finally determined for the comparison experiments. Three sets of welding strategies were compared; of these, the welding parameters on the front side of Case 2 matched with those of Case 1; however, those on the back differed. According to the control experiments, the effects of different reverse-side welding parameters on the weld properties under identical front-side welding processes were compared. Case 3 was compared with Case 1, and the effects of different welding speeds on the welding properties were compared.

3 Numerical simulation

3.1 Numerical model

To establish a more accurate mathematical model for describing the physical process of laser double-sided welding with filler wire, the CFD method was used to model and compute the laser double-sided welding with filler wire. Compared with the finite element method (which only considers heat conduction), the fluid dynamics framework can describe the flow and convective heat transfer inside the weld pool, and it can simulate the weld seam shape via a multiphase flow model.

Table 2: Welding parameters of different cases

		Case 1	Case 2	Case 3
Front side	Welding speed (mm⋅s ⁻¹)	4	4	3
	Wire feeding speed (mm·s ⁻¹)	5	5	5
Reverse side	Welding speed (mm·s ⁻¹)	4	4	3
	Wire feeding speed (mm·s ⁻¹)	5	3	5

The multiphase flow model was used to track the free surface of the workpiece to distinguish the atmospheric environment from the workpiece. The volume of fluid (VOF) is a simple and effective method for multiphase flow interface tracking; it is expressed by [22,23].

$$\frac{\partial F}{\partial t} + \overrightarrow{u} \cdot \nabla F = 0. \tag{1}$$

In this equation, F describes the dynamic evolution of different phases and it must satisfy the condition of $F_{\mathrm{phase1}} + F_{\mathrm{phase1}} = 1$. When the first phase only exists at this position, $F_{\mathrm{phase1}} + 1$, and $F_{\mathrm{phase2}} = 0$. In contrast, when the second phase only exists at this position, $F_{\mathrm{phase1}} = 0$, and $F_{\mathrm{phase2}} = 1$. At the interface of the two phases, F_{phase1} and F_{phase2} are less than 1 and greater than 0. In the numerical model, air was defined as the first phase and the workpiece was defined as the second phase.

By solving the phase volume fraction, the positions of the two phases in space were obtained. For the VOF method, different phases share the same momentum equation, and each phase need not be solved separately. The VOF equation and momentum equation were coupled via the density function. The flow parameters in the weld pool were obtained by solving the momentum equation. In the VOF method, the density at the single-phase position was the material density; meanwhile, the density at the free interface was the mixed density of the two phases.

The mass transfer process in the computational domain was solved by the mass equation, which strictly obeys the mass conservation law:

$$\frac{\partial \rho}{\partial t} + \rho \nabla \cdot \overrightarrow{u} = 0. \tag{2}$$

Here, \overrightarrow{u} is the velocity and ρ is the material density. At the two-phase interface, the density satisfies $\rho = F_{\text{phase}1}\rho_1 + F_{\text{phase}2}\rho_2$.

In the three-dimensional transient heat-fluid coupling numerical model of laser welding with filler wire, the VOF method was used to trace the interface between metal and air. Through redevelopment technology, the momentum equation source terms (e.g., recoil pressure and surface tension) were introduced into the interface. In the global computational domain, the momentum equation source terms (e.g., the Darcy resistance, gravity, thermal buoyancy, and latent heat absorption of melting and solidification) were introduced as the energy equation source terms. The adaptive heat source model, radiation, and convection were used in the interface as the energy equation source terms.

In the numerical model, the flow in the weld pool was calculated via the momentum equation

$$\rho \frac{\partial}{\partial t}(\overrightarrow{u}) + \rho \nabla \cdot (\overrightarrow{u} \overrightarrow{u}) = -\nabla p + \mu \nabla \cdot (\nabla \overrightarrow{u}) + S_{\overrightarrow{u}}.$$
 (3)

Here, $S_{\overrightarrow{u}}$ is the source term and is used to introduce the applied forces, including gravity, buoyancy, surface tension, recoil pressure, and Darcy resistance, to reflect solidification. The expression is as follows:

$$S_{\overrightarrow{u}} = S_g + S_\sigma + S_r + S_k + S_f. \tag{4}$$

In the calculation domain, the heat conduction and heat convection in the weld are calculated by the energy equation

$$\rho \frac{\partial h}{\partial t} + \rho \overrightarrow{u} \nabla \cdot h = k \nabla \cdot (\nabla T) + S_{h}. \tag{5}$$

Here, S_h is the source term of the energy equation and includes the laser heat source, melting latent heat, surface radiation, and surface convection. The expression is as follows:

$$S_{\rm h} = S_{\rm re} + S_{\rm L} + S_{\rm c} + S_{\rm laser}. \tag{6}$$

For the whole computational domain, we determined which locations in the computing domain were required to consider the effects of different forces and energy by using logical judgment statements in the secondary development interface. Surface tension and recoil pressure only act upon and in a direction perpendicular to the phase interface. Similarly, the energy variation caused by surface radiation and surface convective heat transfer only occurs at the phase interface. During the cyclic retrieval of the computing domain, the phase interface area was determined by the logical judgment statement. The surface tension and recoil pressure were loaded into the precession equation, and the surface radiation and surface convection were loaded into the energy equation.

The surface tension is calculated by the continuous surface tension model [24]. The expression is defined as

$$S_{\sigma} = \nabla \cdot \left(\frac{\nabla F}{|\nabla F|}\right) (\sigma - 0.00035\Delta T), \tag{7}$$

where σ is the surface tension and is shown in Table 3.

The recoil pressure is produced by metal evaporation and its expression is

$$S_{\rm r} = 0.55 B_{\rm o} T^{\frac{1}{2}} e^{M_{\rm a} L_{\rm v} / N_{\rm a} k_{\rm b} / T}. \tag{8}$$

In this equation, M_a is the material atomic mass, L_v is the latent heat of evaporation, N_a is Avogadro's number, k_b is Boltzmann's constant, and $B_0 = 2.05 \times 10^{12}$ for aluminum [25].

Surface radiation is calculated by the following formula:

$$S_{\rm re} = \theta \delta_0 (T^4 - T_{\rm r}^4), \tag{9}$$

Table 3: Material parameters

Properties of 2195 Al–Li alloys					
Density ρ	2,710 kg·m ⁻³				
Thermal conductivity <i>k</i>	$ \begin{cases} -0.07T + 259.61, \ T < T_L \\ 0.0283T + 62.547, \ T > T_L \end{cases} W \cdot (m \cdot K)^{-1} [28] $				
Viscosity μ	(-0.0015 T + 2.8) mPa·s [29]				
Melting latent	$398,000 \text{J-kg}^{-1}$				
heat $L_{\rm m}$					
Liquidus	960 K				
temperature T_L					
Solidus	920 K				
temperature T_S					
Expansion	$2 \times 10^{-5} \text{K}^{-1}$				
coefficient $oldsymbol{eta}$					
Surface tension σ	0.7 N·m ⁻¹				

where $\delta_0 = 5.6697 \times 10^{-8}$ is the Stefan–Boltzmann constant and θ denotes the emissivity.

The convective heat loss was defined as

$$S_{\rm c} = h_{\rm c}(T - T_{\rm r}), \tag{10}$$

where h_c is the convection heat transfer coefficient, which considers the energy loss produced by the convection of protective gas, and was set to 160.

Unlike the aforementioned force and energy changes (which only act on the phase interface), these effects were located in the whole calculation domain. Thermal buoyancy and gravity are loaded in the *z*-direction momentum equation, and the Darcy damp force (reflecting solidification) was loaded in the region below the melting point. Similarly, the latent heat was loaded at the position just below the melting point, and the laser heat source was activated at the focus position; these were added to the source term of the energy equation.

The source term of gravity was defined as

$$S_{g} = -\rho g, \tag{11}$$

where *g* is the acceleration due to gravity. The thermal buoyancy was defined as

$$S_{\rm f} = \rho g \beta (T - T_{\rm r}), \tag{12}$$

where β is the thermal expansion coefficient (defined as in Table 3) and $T_{\rm r}$ = 300 K.

By introducing a very large damping force, the flow in the region below the melting point was halted and then simulated as a solid. To achieve this, we used enthalpyporous technology in the model [26]. This damping force can be expressed as

$$S_{\rm k} = -c \frac{(1 - f_{\rm L})^2}{f_{\rm L}^3 + b} \cdot \overrightarrow{u}, f_{\rm L} = \frac{T - T_{\rm S}}{T_{\rm L} - T_{\rm S}},$$
 (13)

where $c = 1 \times 10^5 - 1 \times 10^8$, $T_{\rm S}$ is the solidus temperature, $T_{\rm L}$ is the liquidus temperature, $L_{\rm m}$ is the latent heat of the melt, and $T_{\rm m}$ is the melting temperature.

The latent heat of melting can be defined as

$$S_{\rm L} = -\nabla(\rho u_i f_{\rm L} L_{\rm m}), \quad T > T_{\rm m}, \tag{14}$$

where $L_{\rm m}$ is the latent heat of the melt, and $T_{\rm m}$ is the melting temperature; these are shown in Table 3.

The laser source was based upon a Rotary Gauss body heat source model [27]

$$S_{\text{laser}} = \frac{9P_{\text{laser}}\eta}{\pi H(t)R_0^2(1-10^{-3})} \exp\left[\frac{-9(x^2+y^2)}{R_0^2 \ln(H(t)/z)}\right].$$
(15)

Here, R_0 is the laser beam radius, η is the absorption rate of Al–Li alloy (set as 0.4), and H(t) is the deepest depth of the phase interface, which was returned by the VOF solver for every time step.

All the aforementioned material-related parameters are shown in Table 3.

To simplify the model and accelerate calculation, the following assumptions were set:

- (1) The Al–Li alloy butt joints were replaced with a complete plate in the computational domain.
- (2) The surface tension and thermal conductivity viscosity of the Al–Li alloys were set as functions of temperature, and other thermal properties were set as temperature-independent constants.
- (3) The flow state of the liquid metal was that of the laminar flow.

3.2 Material characteristics and computational domain

As shown in Figure 3, the computational domain was covered by a hexahedral mesh and divided into three regions. The upper and lower regions were defined as air phases, and the middle region was the workpiece (thickness: $2\,\mathrm{mm}$); the size of the computational domain was $8\,\mathrm{mm} \times 8\,\mathrm{mm} \times 7\,\mathrm{mm}$. At the top and bottom of the computational domain, a mobile welding wire inlet corresponding to the ambient temperature was established. The inlet speed was consistent with the wire feeding speed, and the welding wire entered the calculation domain in the form of a liquid column to allow the heat and mass transfer of the welding wire in the melting process to be simulated.

As a workpiece, the physical parameters of the 2195 Al–Li alloys included thermal conductivity, specific heat capacity, viscosity, latent heat of melting, and so on. In the actual welding process, the flow of the liquid metal

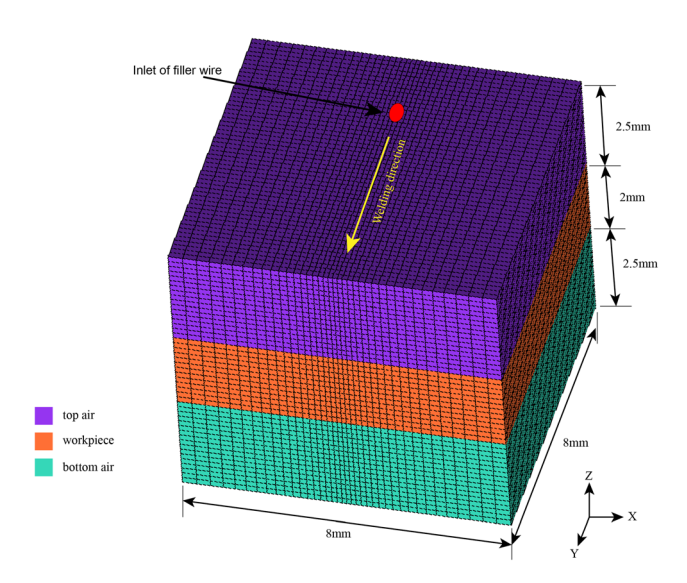


Figure 3: Diagram of the computational domain.

considerably determines the heat transfer and weld morphology in the weld pool. Through the user-defined function in FLUNT software, the source terms of the energy and momentum equations were introduced into the computational domain using the secondary development method, and the material parameters were set as a function of temperature.

3.3 Verification and analysis of simulation results

After the welding began, the heat absorption of the welding wire meant that a portion of the heat of the weld pool was transferred to the welding wire, resulting in the energy decrease of the former. Thus, although the recoil pressure generated by the evaporation of the liquid metal was considered in the numerical model, the simulation results show that only very shallow keyholes were formed on the surface of the weld pool, as shown in Figure 4(a). The welding mode was thermal conduction welding, and deep penetration welding did not occur. Figure 4 shows the three-dimensional results of the welding process. The weld FZ boundary of the cross section obtained in the experiment was compared with the simulation results after reaching the quasi-steady state; the two were essentially consistent, which verifies the reliability of the numerical simulation results.

The simulation results of the weld cross section were consistent with the experimental results. Comparing the different results in Figure 4, we see that, under the same laser power, slower welding speeds increased the heat input and the depth and width of the FZ. Increasing the wire feed speed led to an increase in the heat absorption of the wire, a decrease in the energy input to the weld and a decrease in the FZ. Compared with other cases, the FZ of Case 3 was the widest, and the FZ boundary was almost perpendicular to the workpiece plane; the FZ shape in the other two cases resembled the symmetrical superposition of two semi-ellipses. The extremity of Case 3 shows that the role of convective heat transfer cannot be neglected in the heat transfer of the weld pool. When welding began, the surface of the workpiece was rapidly heated and melted to form a weld pool. Then, the liquid metal in the weld pool was squeezed around the weld pool under the action of Marangoni convection. The flowing metal transferred the laser energy to the edge of the weld pool via convection, and the unmelted solid metal at the edge of the weld pool was heated by the contacting melt, increasing the melting width. Figure 5 shows the velocity field in the cross-sectional area of the weld at the focal point of the laser under different cases. The velocity vector in the area was marked by an arrow. Case 3 penetrated the weld of the other side; hence, only the flow field of the second weld was studied.

As can be seen from the longitudinal section flow field of the weld in Figure 5, the liquid metal in the middle of the weld pool flowed downward and was deflected at the bottom of the weld pool, forming reflux along its boundary. According to the factors considered in the numerical model for the weld pool, this phenomenon was caused by Marangoni convection, thermal buoyancy, gravity, and so on. The thermal buoyancy flow was produced by temperature-change-induced density differences. Marangoni convection was caused by the surface tension gradient produced by the different surface tensions at different locations. Under the action of surface tension, gravity, and recoil pressure, the liquid metal flowed downward from the surface to the bottom of the weld pool. However, the metal below the weld pool was not melted and still existed in a solid form. Because it was blocked by a solid metal, the liquid metal at the bottom of the weld pool was directed to flow around, and a portion returned to the surface of the weld pool and solidified, forming the reflux.

4 Results and discussion

4.1 Macrostructure of the joints

Because the two sides of the workpiece were welded asynchronously in the experiment, one-pass welding was performed on each side; thus, the upper surface of

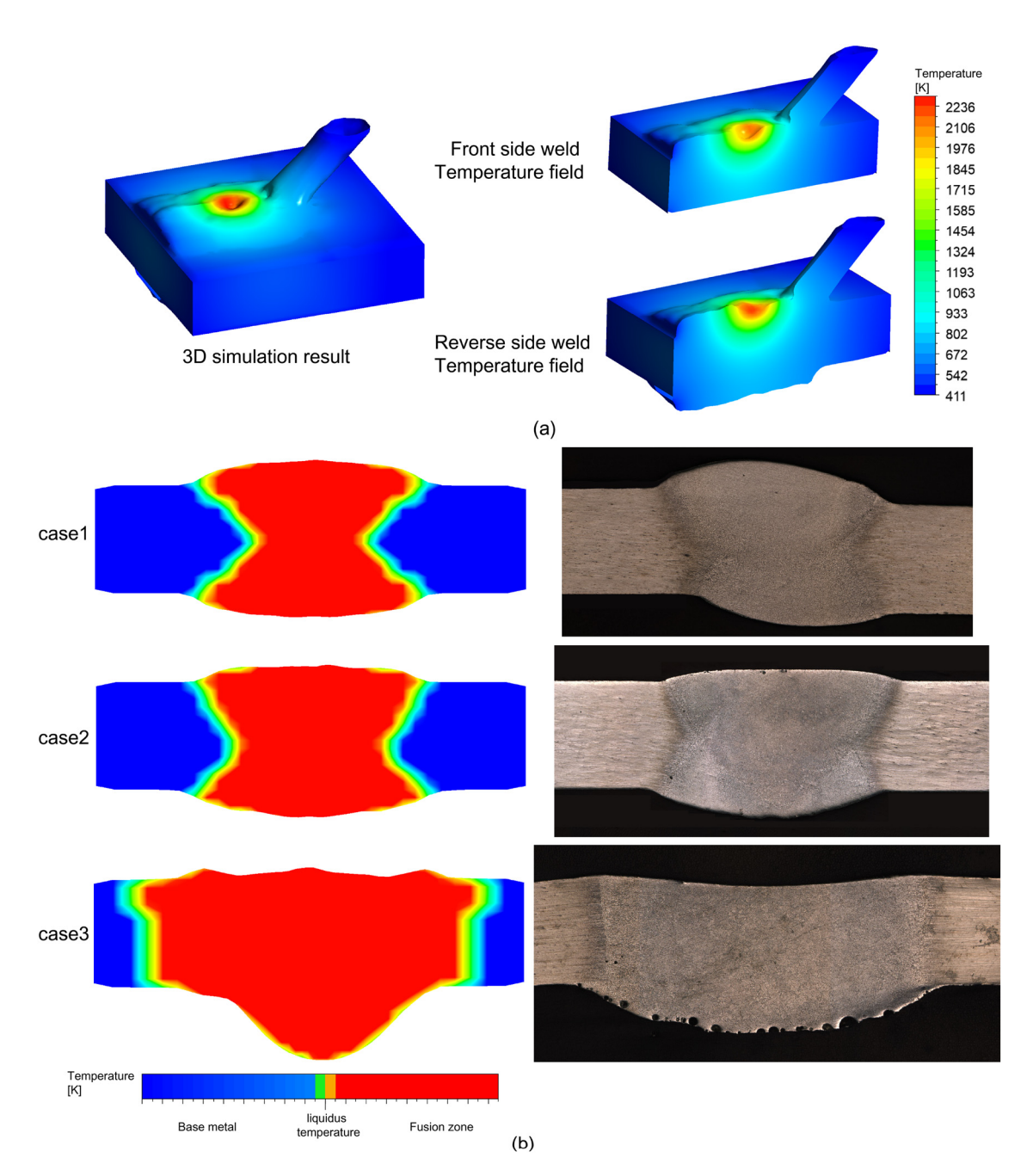


Figure 4: Experiment and simulation results. (a) Temperature field in the weld; (b) the fusion zone of the simulation and the experiment.

the plate was set as the front side to perform the first weld, and the lower surface was set as the reverse side to perform the second. Figures 6–8 depict the microstructures of Cases 1, 2, and 3, respectively. The upper weld was the second weld on the reverse side, and the lower was the first weld on the front side. Because the workpiece material used was 2195-T8 Al–Li alloy, the original microstructure of the base metal (BM) was that of a long rolling-aged state. The process parameters on the front and reverse sides of Case 1 were identical, and the macro-

morphology is visible in Figure 6(a). The FZ shape was superimposed by two ellipses symmetrically along the horizontal line of the weld center. The FZ of the front welding overlapped slightly with the HAZ/partially melted zone (PMZ) of the back welding; thus, there was no guarantee that the weld was penetrated. Gaps may be present in the HAZ/PMZ, and no obvious pores and cracks were observed inside the FZ or on the edge of the weld. The evolution of the welded joint microstructures from HAZ to weld center was characterized by BM, HAZ, PMZ, a

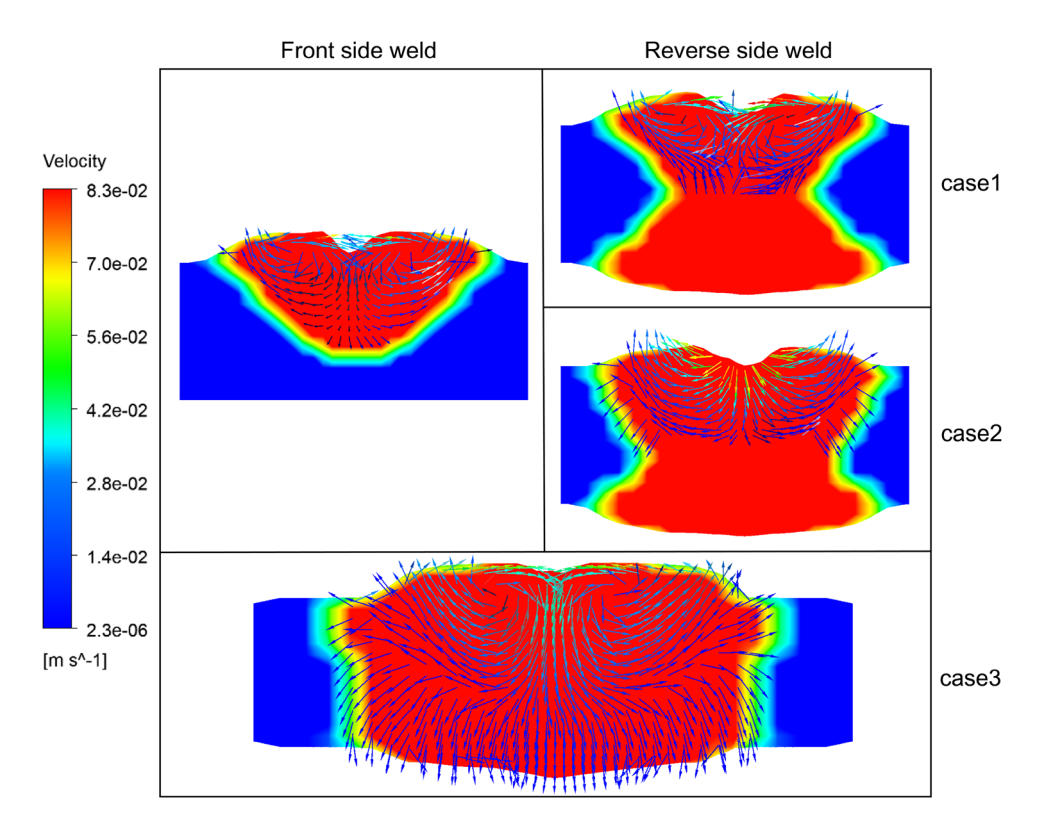


Figure 5: The velocity field of the weld pool.

columnar grain zone, and a mixed zone of equiaxed dendrites and equiaxed grains with a coarse rolling-aged microstructure. In Figure 6(b) and (d), a clear columnar

grain structure can be observed at the FZ boundary, attributable to the large temperature gradient in this area; this made the crystal grains grow epitaxially along the

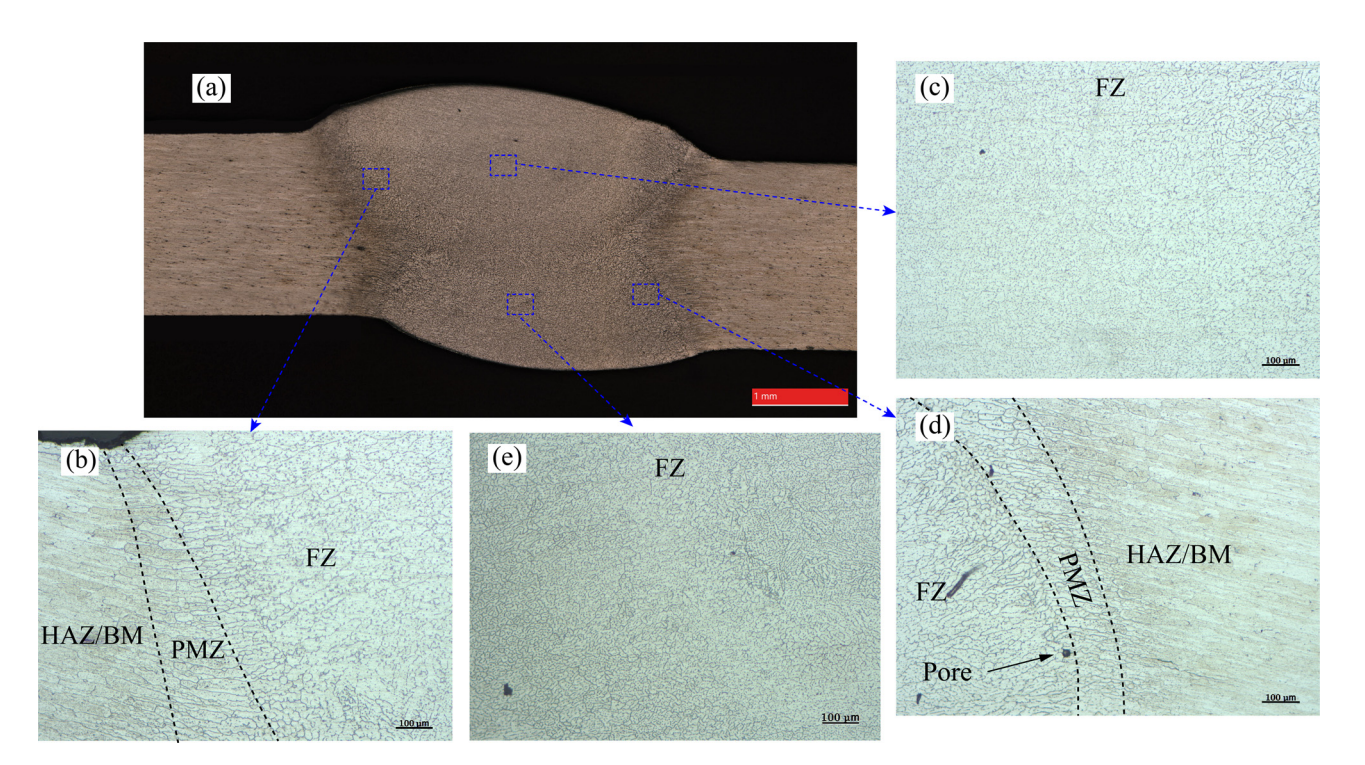


Figure 6: Case 1: metallographic structure.

solidification front [30,31]. Nearer to the weld center, the temperature gradient in the weld decreased, and the columnar crystals were converted into equiaxed grain and equiaxed dendrites [1,32–34].

From the equiaxed grain structure welded on the back side (Figure 6(c)) and the equiaxed grain structure on the front weld (Figure 6(e)), it can be seen that the grain size of the first weld on the front side did not significantly differ from that of the second weld on the back. Comparing the front and back welds in Figure 6(c) and (e), it can be seen that not only the columnar grain zone of the weld and the widths of the PMZ and HAZ are identical, but also the multiple crystal forms at the FZ boundary are also consistent. Because the welding parameters on the front side matched those on the back side, the heat input was identical. This may affect the cooling rate of the workpiece, owing to the change in the geometry of the weld height after the end of the first weld; however, the influencing factor is negligibly small. The columnar grains on the upper portion of the weld were transformed into fine equiaxed dendrites, and the middle equiaxed dendrites were mixed with coarse equiaxed grains. The welding center exhibited a mixed zone of equiaxed dendrites and equiaxed grains, the grain size gradually decreased from the upper to the lower parts of the weld, and the middle grain size was slightly larger than the upper and lower parts. This was mainly caused by the higher temperatures in the upper region of the weld pool.

Figure 7(a) shows the macro morphology of Case 2. Because the welding speed of the first and second welds was 4 mm·s⁻¹, the wire feeding speeds of the front and back were 5 and 3 mm·s⁻¹. The heat input of the welding on both sides remained relatively constant, and the widths of the two welds' macro morphologies were very close. When the composition of the welding wire remained unchanged, the morphology of the front did not differ notably from that of the back. The most obvious difference was that the wire feeding speed on the front exceeded that on the back, resulting in a higher weld reinforcement on the front. Compared with Figures 5 and 6, the weld shapes and crystallization distributions of the two experiments were very similar, owing to the similar process parameters. Their evolution from the boundary to weld center was followed by HAZ, PMZ, columnar grain zone, and mixing zone of equiaxed dendrites and equiaxed grains. In addition, Figure 7(a) clearly shows that the penetration depth of the back weld in Case 2 was deeper than that of the back weld in Figure 7(a). This was mainly due to the reduction of the wire feeding speed on the back of Case 2, which led to a decrease in the heat absorption of the welding wire. The heat input transferred to the weld pool increased compared to that in Case 1, increasing the penetration and

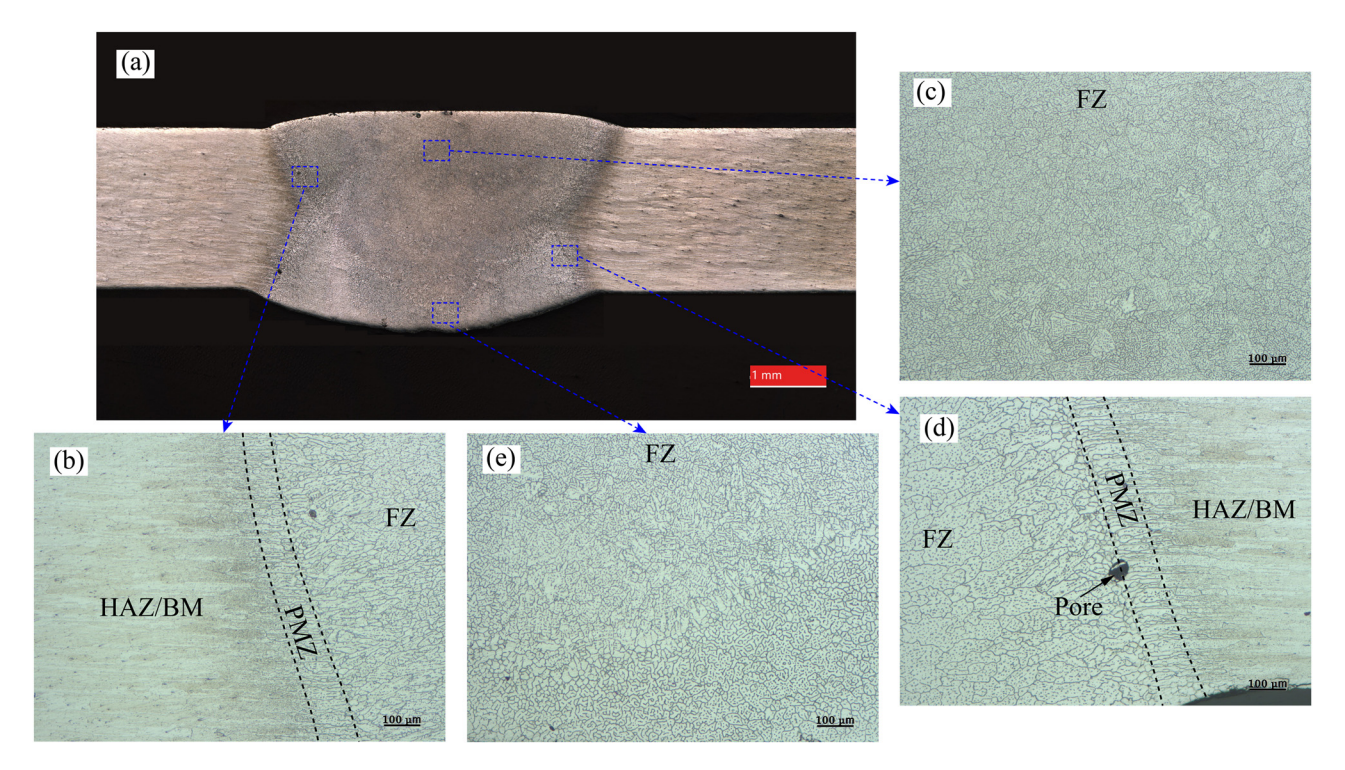


Figure 7: Case 2: metallographic structure.

coarsening of crystal grains. As a result, the sizes of equiaxed grains and equiaxed dendrites in Figure 7(c) exceeded the grain size in Figure 7(e).

Figure 7(a) indicates that a small number of pores were generated at the boundary between the weld and air and the area of contact at the FZ-HAZ boundary. In the mechanical performance test, the locations of the pores and cracks became the weak areas of the mechanical performance, and fractures readily occurred at these positions before rapidly extending to the entire weld [35,36]; in Figure 7(b) and (d), the pores in the HAZ are primarily distributed along the growth direction of the columnar gain. It is speculated that the pores are formed by the sudden decrease in the solubility of hydrogen in the weld metal during the solidification process, which caused the hydrogen bubbles to overflow from the weld center [37-39]. When these escaped to the columnar grain area, the dendrites became solidified and the bubbles could only move along the dendrite gaps. When the temperature was cooled to the point at which the dendrite interstitial was also solidified, the bubbles could not move and remained in situ to form pores.

The welding speed under a constant welding power was lowest in Case 3; hence, the heat input was here highest among all experiments. As can be seen from Figure 8(a), when the first weld was completed, the

second weld on the reverse side directly melted the workpiece owing to its excessive heat input; thus, the recrystallized area of the first weld was remelted and the weld collapsed. Therefore, it is difficult to distinguish the area of the first weld from that of the second.

Compared with Cases 1 and 2, the crystal grain of Case 3 was larger owing to the increase of heat input. Unlike other experiments, a narrow fine equiaxed zone (EQZ) was observed at the FZ boundary in Case 3. As shown in Figure 8(b) and (d), this zone was composed of small equiaxed unit cells. EQZ is considered to be formed by a nonuniform homogeneous nucleation mechanism, with precipitates such as Al₃(Li,Zr) and Al₃Zr acting as potential heterogeneous nucleation sites of EQZ grains, facilitating the formation of an EQZ [40,41].

Compared with Figure 6 for Case 2, numerous hydrogen holes were observed at the bottom of the weld in Figure 7(a) and (e); meanwhile, the pores in other positions essentially matched those in Case 2. This was because the second weld was in a fully penetrated state, and no protective gas was added to the other side of the weld. During the welding process, a large quantity of air was in contact with the bottom weld pool. Therefore, the hydrogen element primarily originated from the absorption of the surrounding water by the alumina on the surface of the workpiece, which caused the supersaturated

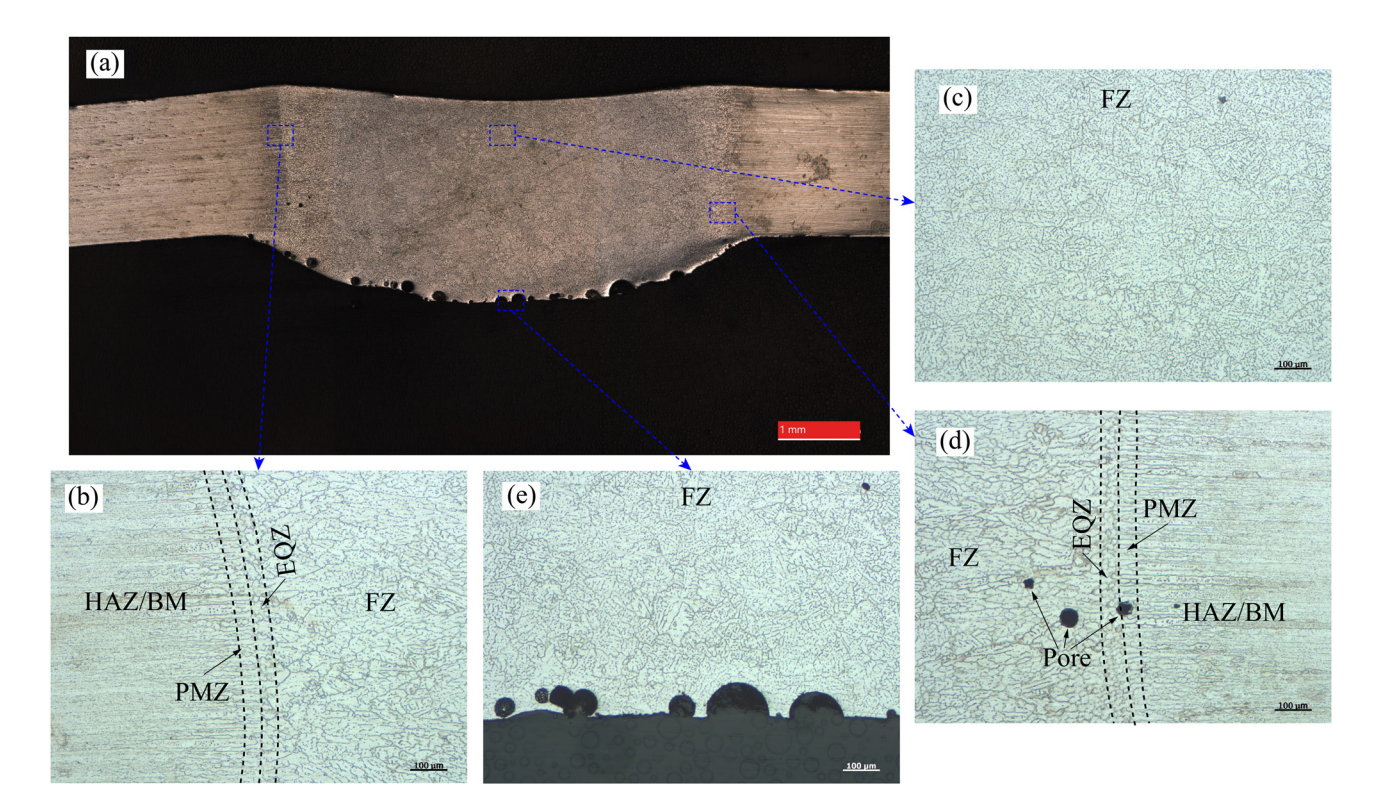


Figure 8: Case 3: metallographic structure.

hydrogen in the FZ to generate hydrogen pores [42]. During solidification, under the rapid decrease of hydrogen solubility, hydrogen overflowed from the bottom, and the air bubbles that were too late to overflow remained on the surface to form surface and subcutaneous pores nearby. To summarize, when the welding speed decreased, the heat input increased, which led to an increase in the number of pores, further increasing the porosity in the weld. A large number of pores reduced the mechanical properties.

Figure 9 shows the width of the weld seam in different cases. The widths of the three different positions in Cases 1 and 2 were relatively similar. However, the widths of the weld seam at the top, middle, and bottom in Case 3 were much larger than those of Case 2. Through calculation, the weld widths at the top, middle, and bottom of the weld seam in Case 3 were increased by 25.36, 74.82, and 28.47%, respectively, compared with those of Case 2. The decrease in the weld seam width entailed a decrease in the heat input. The lower the heat input, the shorter the residence time of the weld seam at high temperatures, the smaller the structure, and the less significant the softening of the HAZ; this improved the mechanical properties of the joint.

To summarize, under the three different welding strategies, the crystalline structure at the weld seam center was composed of equiaxed grains and dendrites with irregular grain sizes and shapes; the greater the heat input, the coarser the grain size, the larger the dendrite spacing, and the more extensive the secondary dendrite development; this led to joint softening. Meanwhile, under the increase in heat input, the pore defects in the weld began to increase. In addition, the penetration depth of Case 1 was approximately half the thickness of the plate, and it was easy to avoid penetrating the workpiece and

producing a joint gap when double-sided welding was performed. As can be seen from Figure 7, when the weld was penetrated using the process parameters of Case 2, although pores remained at the fusion line and weld surface, the number of pores was greatly reduced, and the entire welded joint was in a continuous and uniform state. Thus, the microstructure corresponding to the Case 2 welding strategy was optimal in the three experiments.

4.2 Effect of welding parameters on mechanical properties

Figure 10(a) shows the microhardness distribution of the weld under the three process settings. The hardness test was conducted at the horizontal axis of the workpiece center, and the test result curves at different positions were obtained. According to the curve in Figure 9(b), the microhardness values of the weld under all the three welding parameters presented a W-shaped distribution. The hardness of BM was highest, those HAZ and PMZ were higher than that of FZ, and that of FZ was lowest; this is consistent with the results obtained from similar studies [43]. For Al–Li alloys, the strengthening phases were mainly T-(AlLiSi) and θ -(Al₂Cu) phases, which were dispersed in the matrix, grain boundaries, and dislocations. These dispersion phases pinned the grain boundaries and hindered the motion of dislocations [44].

There are two main causes for the softening of Al–Li weld joints: (1) the dissolution of reinforcing phase particles, the increase of reinforcing phase particle sizes, and the decrease of density distribution, which weakens the dispersion strengthening effect [45]; and (2) the

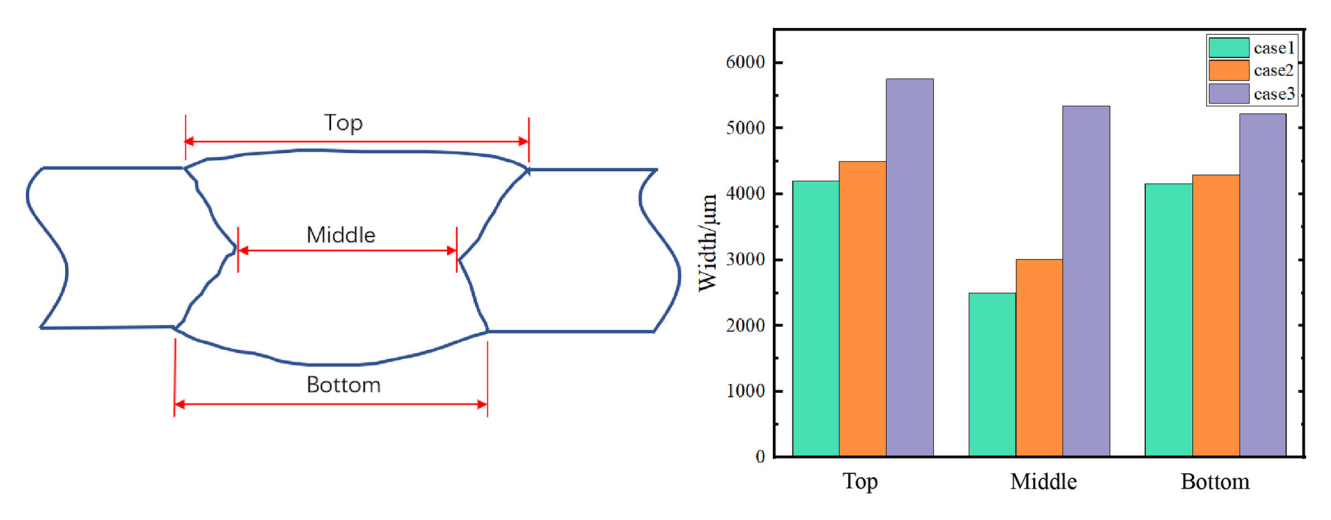


Figure 9: Width of the weld seam of different cases.

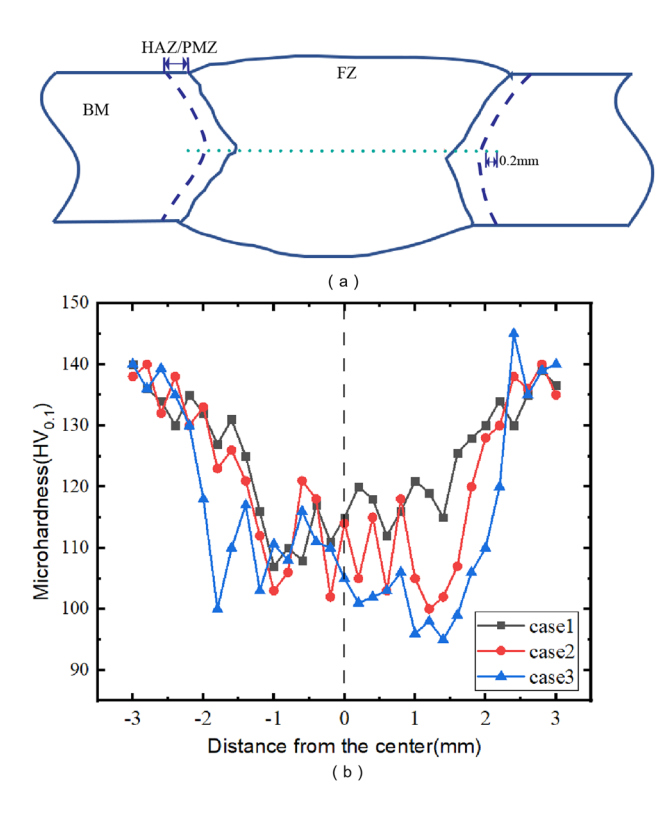


Figure 10: Microhardness of the weld. (a) Location of hardness test; (b) the curve of hardness.

evaporation loss of alloy elements such as Cu, Mg, and Zn [46]. The hardness of 2198/2060 Al–Li alloy was studied in references [32, 34], where it was found that the hardness of the weld was considerably lower than that of the BM (i.e., only half thereof). Compared with their results, the weld hardness in this study could reach 75% of the BM hardness. The reason for this difference was that their research adopted single-sided welding, and the laser power was large; as a result, the dispersion strengthening effect was weakened and the loss of alloying elements was more serious.

During the welding process, owing to the high energy input of the laser, the Cu and Li elements in the upper region of the weld pool evaporated and were lost, which affected the precipitation of the strengthening phase. Combined with the weld pool flow field in Figure 5, the melt containing lost elements flowed to the lower region of the weld pool, reducing the strengthening phases on the surface of the weld pool, which may be one reason for the reduced hardness of the weld center. Comparing the microhardnesses under the three different welding settings, we see that at a faster welding speed and identical laser power, the lower the energy input to the workpiece, the lower the peak temperature of the welding thermal cycle; this results in a decreased joint softening and increased hardness. For Case 3, owing to the slow

welding speed, the heat input increased compared with the other cases, which greatly increased the width of the HAZ. Meanwhile, the coarse grain led to the softening of weld joints, making the hardness of Case 3 the lowest. In addition, the wire feeding speed of Case 2 was reduced during the back welding; thus, when the heat input increased, the joint softening exceeded that of Case 1 at identical welding speeds, and the hardness was reduced.

Figure 11 shows the stress-strain curves of different cases and the corresponding tensile fracture samples. The fracture in Case 1 occurred at the welded joint, and the heat input of Case 1 was the smallest, reducing the depth of the weld pool; thus, the workpiece was not penetrated in the first weld. In the experiment, the two plates were butt connected, and the fluidity of the liquid metal at the edge of the weld pool was reduced by the lack of penetration and the low heat input. The overlapping area of the two weld seams was too small, the joint gap of the flat plate was not completely filled, and a micro gap was generated. This may explain why the strength in Case 1 was lower than that of Case 2. Under similar welding heat input conditions, the penetration depth of the second weld seam increased; thus, the joint was completely penetrated. Even when only a few pores were present, the welding quality was improved. Case 3 was in a fully penetrated state; however, excessive heat input caused the HAZ to expand, the crystal grains to significantly coarsen, and the pores on the back to become an area of mechanical weakness; this became the crack initiation point in the tensile test and promoted the formation and expansion of cracks. The fracture positions of the three cases were observed, and it was found that the fractures occurred near the HAZ, which was consistent with the results of Zhang et al. [34]. In this study, the scanning electron microscopy (SEM) result of the fracture showed that the fracture mode was that of an intergranular fracture. Related research has found that alloying element segregation or intergranular coarse phases can weaken the grain boundary, thereby causing intergranular fracture [47,48]. The fracture location of Case 2 was close to that of Case 1, whereas that of Case 3 was closer to the FZ boundary. In Figure 8, the EQZ can be observed in this region. Gutierrez and Lippold [49] proposed that the EQZ plays a key role in weld crack and fracture sensitivity. Hu et al. [37] proved this view: they observed that the fracture of the Al-Li alloy weld always occurred near the EQZ, and they proposed that the EQZ is the reason for the reduction of crack resistance and the degradation of mechanical properties under static loads. Therefore, the fracture in Case 3 most likely occurred at the EQZ. Thus, it can be clearly seen in Figure 11 that,

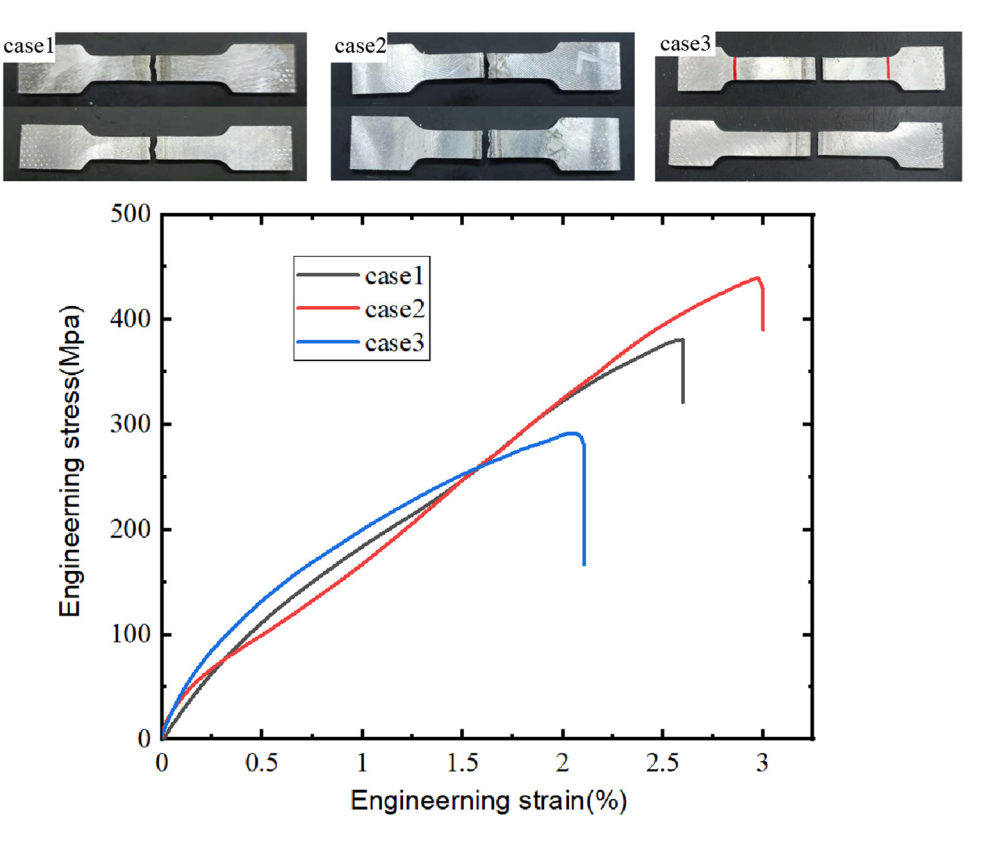


Figure 11: Stress-strain curve for different cases.

compared with other cases, the strength of Case 3 was reduced by the presence of an EQZ.

The tensile strength and elongation of the 2195-T8 Al-Li alloy workpiece at room temperatures were 608 MPa and 9.22%, respectively. Compared with the tensile strength curve in Figure 11, we can see that under the three cases, the sample broke suddenly after reaching the maximum value, and the fractured state was that of brittle fracture. In Case 3, excessive secondary heat inputs led to the expansion of the welding HAZ and serious joint softening. In addition, the stress concentration produced by the pores on the weld surface further reduced the mechanical properties, and the joint strength was the lowest, only 285 MPa (46.8% of that of the workpiece); the process parameters of Case 1 reduced the welding heat input and welding defects. However, this cannot ensure complete penetration and can leave gaps, resulting in a strength decrease. The final tensile strength remained at 381 MPa (62.6% that of the workpiece). The joint strength in the Case 2 sample was 420 MPa (69% of that of the workpiece); that is, no serious joint softening (as observed in Case 3) occurred, the void fraction of the weld was low, and fewer defects were formed. Compared with the Case 1 sample at similar heat input, the strength was increased by 10%, and it exhibited the optimal mechanical properties among all the samples.

In the three cases, the excessive heat input of Case 3 caused the weld to collapse. In the second weld process, the FZ of the first weld melted, and the crystalline structure of that first weld was no longer present. The welding effect of Case 3 was similar to that of single-sided welding, and the expected effect of double-sided welding could not be achieved. In this study, the welding process was numerically simulated. Although the numerical simulation may differ from the actual situation, the variation trend of the numerical results resembled that of the real results [50]. In the simulation and comparison of experimental results in Figure 4, the simulation results are seen to reproduce the collapse process, and the data obtained from the simulation are of great help in analyzing the laws between heat input and mechanical properties. Figure 12 shows the welding thermal cycle curve and cooling curve at different positions in the weld, as obtained from the simulation results. The temperature and cooling rate data for multiple points on the weld cross section were extracted, and the positions of the extraction points in the three cases were identical. To compare the thermal cycle curves of the front and reverse side welds, three points located on the workpiece surface and at the center of the cross section were sampled during the first and second welding processes. The three points corresponded to Points 1, 2, and 3 in

106 — Qihang Xv et al.

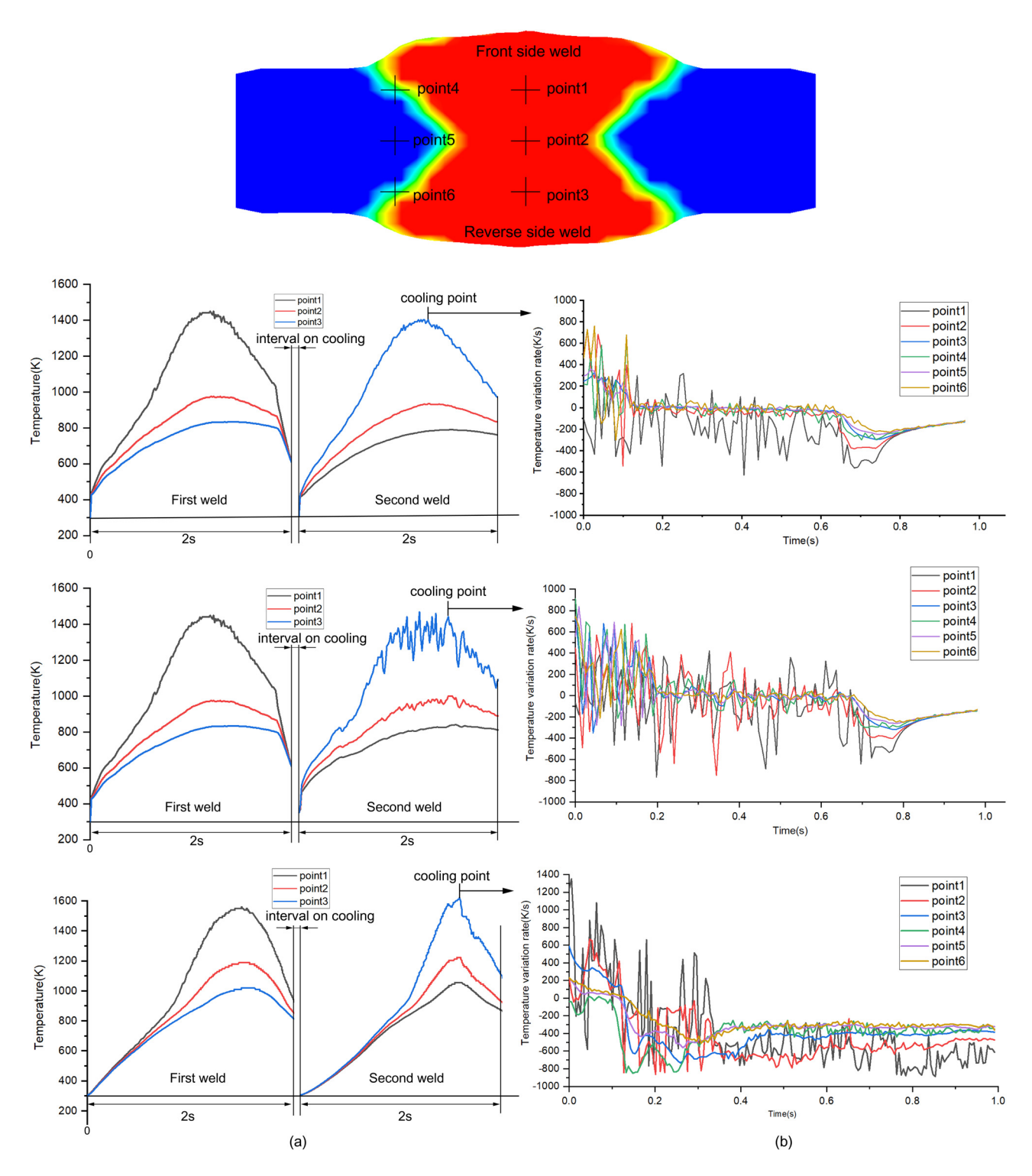


Figure 12: Process of temperature variation: (a) thermal cycle curve in the double-sided weld and (b) temperature variation rate in the cooling stage.

Figure 12. The cooling rate had a significant influence on the mechanical properties of the weld seams. The cooling data of the second weld were sampled and analyzed, and the sample was extracted from the cooling point where the thermal cycle curve entered the cooling zone, marked "cooling point" in Figure 12. To obtain the cooling data for the edge of the weld FZ, three points located at the edge of the weld seam were added for data collection,

corresponding to Points 4, 5, and 6, respectively, in Figure 12; owing to the symmetry of the weld, the thermal data on the mirror side of the three points were essentially consistent with those of the three points.

By comparing the thermal cycle curves in Figure 12, it can be clearly seen that the peak temperature at the three sampling positions in Case 3 is higher than that of the other two cases, with its highest temperature being 1,560 K; this corresponds to the maximum heat input of Case 3. More importantly, the second weld thermal cycle curves of Cases 1 and 2 were very similar, indicating that the heat input of Case 2 was successfully controlled in a range close to that of Case 1. During welding, the closer the sampling point was to the surface of the weld pool, the higher its temperature. The distances between the three points sampled for thermal cycle temperature measurement were identical; however, the simultaneous temperature difference reflects the downward trend of the temperature gradient from the surface to the bottom of the weld pool. The first weld processes of Cases 1 and 2 were identical; however, their second weld processes differed. In Figure 12, the heat input of the second weld of Case 2 is larger, and the area of the thermal cycle curve exceeds that of Case 1. Case 3 had the largest heat input; however, Case 3 also took the longest to reach the peak temperature because slow welding speeds increase the time required for the focal point to reach the sampling location. The results in Figure 5 show that convective heat transfer determines the heat accumulation at this point. Although the heat input had a greater impact on the mechanical properties of the weld seam, the impact of the cooling process on the mechanical properties cannot be neglected.

Figure 12(b) shows the cooling rate curve corresponding to the cooling zone in the second weld thermal cycle curve. By comparing the welding parameters and cooling rate curves of Cases 1 and 2, it was found that the average cooling rate was essentially identical when the wire feeding speed was 2 mm·s⁻¹. By comparing the welding parameters and cooling rate curves of Cases 1 and 3, it was found that the difference in the average cooling rate exceeded 100 K·s⁻¹ when the welding speed was increased by 1 mm·s⁻¹. The cooling rates of Points 3 and 6 in the positions closest to the weld surface in the second weld were lower than those of other positions. The locations with the highest average cooling rate were Points 1 and 2, which were at the bottom region of the weld pool, on the central axis of the weld. When these entered the cooling state, the temperature change rate reached approximately -500 K·s⁻¹; meanwhile, the temperature change rate of the other four points was 50% that of these

two points. Point 2 was located at the edge of the weld pool, where the cooling rate of Case 2 exceeded that of Case 1, and the temperature at this point was close to that of Case 1, showing high cooling rates in the crystallization region at the bottom of the weld pool; this also led to a high degree of undercooling and grain refinement in the FZ at the same region. It can be seen in Figure 7(e) that this also caused the intensity of Case 2 to exceed that of Case 1. Because recrystallization did not occur at Point 1, it is not discussed. In addition, the cooling rates of the six positions in Case 3 exceeded those of Cases 1 and 2, which alleviates the coarser grain through excessive heat input. However, this also led to rapid cooling of the weld seam, and the hydrogen did not have sufficient time to overflow the weld pool; thus, pores were formed. The same problem also occurred in Case 2, and Case 3 was the most serious. By comparing the cooling rates of the three cases, the cooling rates of the weld seam are seen to increase under the increase in heat input. High cooling rates also affected the generation of the EQZ at the weld seam edge of Case 3; this also reduced the mechanical properties of Case 3.

To conclude, when double-sided welding was performed, the lower welding heat input reduced the loss of alloying elements in the weld pool, the weld seam microstructure was more refined, and the weld seam hardness was increased. However, with plate butt joints, it is easy to produce an insufficient weld penetration depth, which affects the seam filling and leads to microgaps. Meanwhile, the numerical results show that an increase in heat input produces crystal coarsening and increases the cooling rate; furthermore, the weld seam solidifies before hydrogen overflows from the weld pool. Therefore, the laser power, welding speed, and wire feeding speed must be controlled within a reasonable range to prevent the excessive heat input from penetrating the weld on the other side and producing defects. By comparing the weld properties and process parameters of Cases 2 and 1, it was found that the welding strategy under different process parameters on either side of the workpiece could effectively control the heat input, reduce the occurrence of defects in the weld seam, and increase its mechanical properties.

5 Conclusion

The effects of different welding parameters on the mechanical properties of double-sided laser welding using filler wire were studied by combining experiment and numerical simulation results. A three-dimensional transient

multiphysics numerical model was established to study the effects of temperature and flow on weld performance; the results of the numerical simulation were verified by experiments.

The factors affecting the mechanical properties of the weld were explored by comparing the experimental results and analyzing the numerical simulation ones. This represents a novel research method. It is almost impossible to monitor the temperature variation in the weld via experiment; however, data difficult to obtain in the experiment can be obtained by numerical simulation. Under identical other welding parameters, reducing the welding speed increased the heat input of the weld, which causes an increase in the peak temperature and cooling rate. By comparing the welding parameters with the cooling rate curve, it was found that the peak temperature was essentially consistent with the average cooling rate when the wire feeding speed was increased by 2 mm·s⁻¹. When the welding speed difference was 1 mm·s⁻¹, the peak temperature was 200 K higher than under the higher welding speed, and the average cooling rate was more than 100 K·s⁻¹. By comparing the simulation results with the double-sided welding experiment, it was found that excessive heat input in the weld did more than simply increase the penetration width and depth and melt the first weld: it led to coarse grains in the weld, which increased the hydrogen porosity and reduced the weld's mechanical properties. Therefore, it is highly likely that the quantity of hydrogen porosity will receive a cooling rate, and an increase in cooling rate will lead to an increase in hydrogen porosity. In addition, the comparison results show that the strategy of setting the reverse-side welding process parameters to differ from those of the front side can effectively control the heat input, produce better weld morphologies and microstructures, and increase the weld's mechanical properties. It was found that when the wire feeding speed was 5 mm·s⁻¹ for the first weld and reduced to 3 mm·s⁻¹ for the second, the tensile strength of the weld specimen was increased by 10%. In this work, through a combination of numerical simulations and experiments, the influences of weld parameters on the weld performance were studied using the temperature field simulation results. We believe that this method can quantitatively and intuitively be used to study similar fields and promote the development of welding technology.

Acknowledgements: The authors acknowledge funding from National Natural Science Foundation of China (Grant Number: 92060106) and the Institutional Foundation (Grant Number: 2019QNJJ002).

Funding information: This work was supported by the National Natural Science Foundation of China (Grant Number: 92060106) and the Institutional Foundation (Grant Number: 2019QNJJ002).

Author contributions: Qihang Xv: conceptualization, data curation, formal analysis, writing – original draft, writing – review and editing, methodology, software, investigation; Gan Tian: supervision, writing – original draft, formal analysis, validation, visualization, project administration; Wei Zhang: writing – review and editing, formal analysis, resources; Zhengwei Yang: visualization, writing – review and editing, methodology, Anbo Ming: formal analysis, validation, methodology, writing – review and editing.

Conflict of interest: All authors certify that they have no affiliations with or involvement in any organization or entity with any financial interest or nonfinancial interest in the subject matter or materials discussed in this manuscript.

Data availability statement: The datasets generated during and/or analyzed during the current study are available from the corresponding author on reasonable request.

References

- [1] Zhao, T., Y. S. Sato, R. Xiao, T. Huang, and J. Zhang. Laser pressure welding of Al-Li Alloy 2198: effect of welding parameters on fusion zone characteristics associated with mechanical properties. *High Temperature Materials and Processes*, Vol. 39, No. 1, 2020, pp. 146-156.
- [2] Caiazzo, F., V. Alfieri, F. Cardaropoli, and V. Sergi. Butt autogenous laser welding of AA 2024 aluminium alloy thin sheets with a Yb:YAG disk laser. *The International Journal of Advanced Manufacturing Technology*, Vol. 67, No. 9–12, 2013, pp. 2157–2169.
- [3] Kashaev, N., V. Ventzke, and G. Çam. Prospects of laser beam welding and friction stir welding processes for aluminum airframe structural applications. *Journal of Manufacturing Processes*, Vol. 36, 2018, pp. 571–600.
- [4] Heidarzadeh, A., S. Mironov, R. Kaibyshev, G. Çam, A. Simar, A. Gerlich, et al. Friction stir welding/processing of metals and alloys: a comprehensive review on microstructural evolution. *Progress in Materials Science*, Vol. 117, 2021, id. 100752.
- [5] Çam, G. and G. İpekoğlu. Recent developments in joining of aluminium alloys. The International Journal of Advanced Manufacturing Technology, Vol. 91, No. 5–8, 2017, pp. 1851–1866.
- [6] Çam, G. and M. Koçak. Progress in joining of advanced materials. *International Materials Reviews*, Vol. 43, No. 1, 1998, pp. 1-44.
- [7] Pakdil, M., G. Çam, M. Koçak, and S. Erim. Microstructural and mechanical characterization of laser beam welded AA6056

- Al-alloy. *Materials Science and Engineering: A*, Vol. 528, No. 24, 2011, pp. 7350–7356.
- [8] Çam, G. and M. Koçak. Microstructural and mechanical characterization of electron beam welded Al-alloy 7020. Journal of Materials Science, Vol. 42, No. 17, 2007, pp. 7154–7161.
- [9] Çam, G., V. Ventzke, J. F. Dos Santos, M. Koçak, G. Jennequin, and P. Gonthier-Maurin. Characterisation of electron beam welded aluminium alloys. *Science and Technology of Welding* and Joining, Vol. 4, No. 5, 1999, pp. 317–323.
- [10] Von Strombeck, A., G. Çam, J. F. Dos Santos, V. Ventzke, and M. Koçak. A comparison between microstructure, properties, and toughness behavior of power beam and friction stir welds in Al-Alloys. In: Proceedings of the TMS 2001 Annual Meeting Aluminum, Automotive and Joining (New Orleans, Louisiana, USA, February 12–14, 2001), Das, S. K., Kaufman, J. G., and Lienert T. J., eds., TMS, Warrendale, PA, USA, 2001, pp. 249–264.
- [11] Cam, G., V. Ventzke, J. Santos, M. Kocak, G. Jennequin, P. Maurin, et al. Characterization of laser and electron beam welded Al-alloys. *Practical Metallography*, Vol. 36, No. 2, 1999, pp. 59–89.
- [12] Çam, G. and M. Koçak. Progress in joining of advanced materials Part I: Solid state joining, fusion joining, and joining of intermetallics. *Science and Technology of Welding and Joining*, Vol. 3, No. 3, 1998, pp. 105–126.
- [13] Farrokhi, F. Hybrid laser welding of large steel structures: an experimental and numerical study. Doctoral dissertation, Aalborg University, Aalborg, 2018.
- [14] Zhou, F. M., Z. S. Yu, Y. H. Feng, Y. C. Huang, and Y. Y. Qian. Numerical analysis of heat transfer process for double sided tungsten inert gas – metal inert gas weld pool. *Science and Technology of Welding and Joining*, Vol. 8, No. 1, 2003, pp. 76–78.
- [15] Wu, C. S., J. S. Sun, and Y. M. Zhang. Numerical simulation of dynamic development of Keyhole in double-sided arc welding. Modelling and Simulation in Materials Science and Engineering, Vol. 12, No. 3, 2004, pp. 423–442.
- [16] Dong, H., H. Gao, and L. Wu. Heat transfer and fluid flow in fusion type PA-GTA double-sided welding. *Modelling and Simulation in Materials Science and Engineering*, Vol. 13, No. 8, 2005, pp. 1205–1215.
- [17] Luo, J., Y. Yuan, X. Wang, and Z. Yao. Double-sided single-pass submerged arc welding for 2205 duplex stainless steel. *Journal of Materials Engineering and Performance*, Vol. 22, No. 9, 2013, pp. 2477–2486.
- [18] Lei, Z., K. Zhang, X. Hu, Y. Yang, Y. Chen, and Y. Wu. Improvement of weld characteristics by laser-arc double-sided welding compared to single arc welding. *Journal of Materials Engineering and Performance*, Vol. 24, No. 11, 2015, pp. 4518–4526.
- [19] Hejazi, I. and S. E. Mirsalehi. Effect of pin penetration depth on double-sided friction stir welded joints of AA6061-T913 alloy. *Transactions of Nonferrous Metals Society of China*, Vol. 26, No. 3, 2016, pp. 676-683.
- [20] Jiang, Z., X. Hua, L. Huang, D. Wu, F. Li, and Y. Zhang. Double-sided hybrid laser-MIG welding plus MIG welding of 30-Mm-thick aluminium alloy. *The International Journal of Advanced Manufacturing Technology*, Vol. 97, No. 1–4, 2018, pp. 903–913.

- [21] Tuncel, O. and H. Aydin. A comparison of tensile properties of single-sided and double-sided laser welded DP600 steel sheets. *Materials Science*, Vol. 26, No. 2, 2019, pp. 173–178.
- [22] Liovic, P., J.-L. Liow, and M. Rudman. A volume of fluid (VOF) method for the simulation of metallurgical flows. ISIJ International, Vol. 41, No. 3, 2001, pp. 225–233.
- [23] Hirt, C. W. and B. D. Nichols. Volume of fluid (VOF) method for the dynamics of free boundaries. *Journal of Computational Physics*, Vol. 39, No. 1, 1981, pp. 201–225.
- [24] Brackbill, J. U., D. B. Kothe, and C. Zemach. A continuum method for modeling surface tension. *Journal of Computational Physics*, Vol. 100, No. 2, 1992, pp. 335–354.
- [25] Semak, V. and A. Matsunawa. The role of recoil pressure in energy balance during laser materials processing. *Journal* of Physics D: Applied Physics, Vol. 30, No. 18, 1997, pp. 2541–2552.
- [26] Brent, A. D., V. R. Voller, and K. J. Reid. Enthalpy-porosity technique for modeling convection-diffusion phase change: application to the melting of a pure metal. *Numerical Heat Transfer*, Vol. 13, No. 3, 1988, pp. 297–318.
- [27] Zhao, H., W. Niu, B. Zhang, Y. Lei, M. Kodama, and T. Ishide. Modelling of keyhole dynamics and porosity formation considering the adaptive keyhole shape and three-phase coupling during deep-penetration laser welding. *Journal of Physics D: Applied Physics*, Vol. 44, No. 48, 2011, id. 485302.
- [28] Leitner, M., T. Leitner, A. Schmon, K. Aziz, and G. Pottlacher. Thermophysical properties of liquid aluminum. *Metallurgical and Materials Transactions A*, Vol. 48, No. 6, 2017, pp. 3036–3045.
- [29] Assael, M. J. and K. Kakosimos. Reference data for the density and viscosity of liquid aluminum and liquid iron. *Journal of Physical and Chemical Reference Data*, Vol. 35, No. 1, 2006, id. 16.
- [30] Wei, H. L., J. W. Elmer, and T. DebRoy. Origin of grain orientation during solidification of an aluminum alloy. Acta Materialia, Vol. 115, 2016, pp. 123–131.
- [31] Wei, H. L., J. W. Elmer, and T. DebRoy. Crystal growth during keyhole mode laser welding. *Acta Materialia*, Vol. 133, 2017, pp. 10–20.
- [32] Liu, F., B. Zhou, Y. Mao, C. Huang, Y. Chen, and Z. Wang. Microstructure and mechanical properties of laser welded joints between 2198/2060 Al-Li alloys. *Materials Science and Technology*, Vol. 34, No. 1, 2018, pp. 111–122.
- [33] Enz, J., C. Carrarin, S. Riekehr, V. Ventzke, and N. Kashaev. Hot cracking behaviour of an autogenously laser welded Al-Cu-Li alloy. *The International Journal of Advanced Manufacturing Technology*, Vol. 95, No. 1–4, 2018, pp. 299–310.
- [34] Zhang, X., W. Yang, and R. Xiao. Microstructure and mechanical properties of laser beam welded Al-Li alloy 2060 with Al-Mg filler wire. *Materials and Design*, Vol. 88, 2015, pp. 446-450.
- [35] Zerbst, U., R. A. Ainsworth, H. T. Beier, H. Pisarski, Z. L. Zhang, K. Nikbin, et al. Review on fracture and crack propagation in weldments – a fracture mechanics perspective. *Engineering Fracture Mechanics*, Vol. 132, 2014, pp. 200–276.
- [36] Wu, S. C., C. Yu, P. S. Yu, J. Y. Buffière, L. Helfen, and Y. N. Fu. Corner fatigue cracking behavior of hybrid laser AA7020 welds by Synchrotron X-Ray computed microtomography. *Materials Science and Engineering: A*, Vol. 651, 2016, pp. 604–614.

- [37] Hu, Y. N., S. C. Wu, and L. Chen. Review on failure behaviors of fusion welded high-strength Al Alloys due to fine equiaxed zone. Engineering Fracture Mechanics, Vol. 208, 2019, pp. 45–71.
- [38] Zhao, Y., X. Zhou, T. Liu, Y. Kang, and X. Zhan. Investigate on the porosity morphology and formation mechanism in laser-MIG hybrid welded joint for 5A06 aluminum alloy with Y-shaped groove. *Journal of Manufacturing Processes*, Vol. 57, 2020, pp. 847–856.
- [39] Wu, S. C., C. Yu, W. H. Zhang, Y. N. Fu, and L. Helfen. Porosity induced fatigue damage of laser welded 7075-T6 joints investigated via synchrotron X-ray microtomography. *Science and Technology of Welding and Joining*, Vol. 20, No. 1, 2015, pp. 11–19.
- [40] Kostrivas, A. and J. C. Lippold. Fusion boundary microstructure evolution in aluminium alloys. Welding in the World, Vol. 50, No. 11–12, 2006, pp. 24–34.
- [41] Liu, T., X. Zhan, R. Fu, and D. Liu. Study on the formation mechanism of fine equiaxed grain ribbons along the fusion lines during 2060/2099 Al-Li alloys dual laser-beam synchronous welding process. *Materials Research Express*, Vol. 6, No. 12, 2019, id. 1265a6.
- [42] Kostrivas, A. and J. C. Lippold. Weldability of Li-Bearing aluminium alloys. *International Materials Reviews*, Vol. 44, No. 6, 1999, id. 21.
- [43] Yang, M., J. Lu, H. Wang, Y. Liu, H. Yang, W. Zhang, et al. Effect of the laser power on the microstructure and mechanical properties of the laser-MIG hybrid welding joints of the 2195 Al-Li alloy. *Science and Technology of Welding and Joining*, Vol. 26, No. 1, 2021, pp. 75–83.

- [44] Kim, J.-H., J.-H. Jeun, H.-J. Chun, Y. R. Lee, J.-T. Yoo, J.-H. Yoon, et al. Effect of precipitates on mechanical properties of AA2195. *Journal of Alloys and Compounds*, Vol. 669, 2016, pp. 187–198.
- [45] Hou, K. H. and W. A. Baeslack. Effect of solute segregation on the weld fusion zone microstructure in CO₂ laser beam and gas tungsten arc welds in Al-Li-Cu alloy 2195. *Journal of Materials Science Letters*, Vol. 15, No. 3, 1996, pp. 208-213.
- [46] Wu, S. C., Y. N. Hu, X. P. Song, Y. L. Xue, and J. F. Peng. On the microstructural and mechanical characterization of hybrid laser-welded Al–Zn–Mg–Cu alloys. *Journal of Materials Engineering and Performance*, Vol. 24, No. 4, 2015, pp. 1540–1550.
- [47] Lynch, S. P., B. C. Muddle, and T. Pasang. Ductile-to-brittle fracture transitions in 8090 Al-Li alloys. *Acta Materialia*, Vol. 49, No. 15, 2001, pp. 2863–2874.
- [48] Cui, L., X. Li, D. He, L. Chen, and S. Gong. Effect of Nd:YAG laser welding on microstructure and hardness of an Al-Li based alloy. *Materials Characterization*, Vol. 71, 2012, pp. 95–102.
- [49] Gutierrez, A. and J. C. Lippold. A proposed mechanism for equiaxed grain formation along the fusion boundary in aluminum-copper-lithium alloys. *Welding Journal*, Vol. 77, No. 3, 1998, pp. 123–132.
- [50] Courtois, M., M. Carin, P. Le Masson, S. Gaied, and M. Balabane. Guidelines in the experimental validation of a 3D heat and fluid flow model of Keyhole laser welding. *Journal of Physics D: Applied Physics*, Vol. 49, No. 15, 2016, id. 155503.